HHS Public Access

Quantitative Susceptibility Mapping by Inversion of a Perturbation Field Model: Correlation with Brain Iron in Normal Aging

Clare Poynton[*],
University of California, San Francisco School of Medicine, San Francisco, CA, 94143 USA and at the time of this work was with the Harvard-MIT Division of Health Sciences and Technology (HST), Massachusetts Institute of Technology, Cambridge, MA, 02139 USA, and the Computer Science and Artificial Intelligence Lab, Massachusetts Institute of Technology, Cambridge, MA, 02139 USA.

Mark Jenkinson,
Oxford Centre for Functional Magnetic Resonance Imaging of the Brain (FMRIB), Nuffield Department of Clinical Neuro-sciences, John Radcliffe Hospital, University of Oxford, OX3 9DU UK.

Elfar Adalsteinsson,
Department of Electrical Engineering and Computer Science, Massachusetts Institute of Technology, Cambridge, MA, 02139 USA and also with the Harvard-MIT Division of Health Sciences and Technology (HST) Massachusetts Institute of Technology, Cambridge, MA, 02139.

Edith V. Sullivan,
Department of Psychiatry and Behavioral Sciences, Stanford University School of Medicine, Stanford, CA, 94305 USA.

Adolf Pfefferbaum, and
Department of Psychiatry and Behavioral Sciences, Stanford University School of Medicine, Stanford, CA, 94305 USA and with the Neuroscience Program, SRI International, Menlo Park, CA, 94025 USA.

William Wells III
Surgical Planning Laboratory, Department of Radiology, Harvard Medical School and Brigham and Womens Hospital, Boston, MA, 02115 USA, and also with the Computer Science and Artificial Intelligence Lab, Massachusetts Institute of Technology, Cambridge, MA 02139 USA.

Abstract

There is increasing evidence that iron deposition occurs in specific regions of the brain in normal aging and neurodegenerative disorders such as Parkinson's, Huntington's, and Alzheimer's disease. Iron deposition changes the magnetic susceptibility of tissue, which alters the MR signal phase,

[*]clare.poynton@ucsf.edu..

and allows estimation of susceptibility differences using quantitative susceptibility mapping (QSM).

We present a method for quantifying susceptibility by inversion of a perturbation model, or 'QSIP'. The perturbation model relates phase to susceptibility using a kernel calculated in the spatial domain, in contrast to previous Fourier-based techniques. A tissue/air susceptibility atlas is used to estimate B_0 inhomogeneity. QSIP estimates in young and elderly subjects are compared to postmortem iron estimates, maps of the Field-Dependent Relaxation Rate Increase (FDRI), and the L1-QSM method.

Results for both groups showed excellent agreement with published postmortem data and in-vivo FDRI: statistically significant Spearman correlations ranging from $Rho = 0.905$ to $Rho = 1.00$ were obtained. QSIP also showed improvement over FDRI and L1-QSM: reduced variance in susceptibility estimates and statistically significant group differences were detected in striatal and brainstem nuclei, consistent with age-dependent iron accumulation in these regions.

Keywords

Quantitative susceptibility mapping; brain iron; normal aging; MRI; inverse methods; atlases

I. Introduction

Excessive iron accumulation in specific regions of the brain is implicated in neurodegenerative disorders such as Parkinson's, Alzheimer's, Multiple Sclerosis, and Huntington's disease [1]–[7]. Iron is involved in many cellular functions throughout the body, but its role in the pathophysiology of neurodegenerative disease remains unknown. Postmortem iron concentration varies substantially between brain regions and throughout the lifespan [8]. In-vivo imaging studies have shown that subcortical brain regions accumulate iron at different rates during normal aging [7], [9]–[11], resulting in significantly greater iron deposition relative to young adults [12]. While increasing iron concentration in neurodegenerative disease and normal aging was first described in histopatho-logical studies (a review of these early studies can be found in [13]), non-invasive imaging methods such as MRI and ultrasound are now being applied to study iron distribution in-vivo [9], [10], [14]–[21].

Iron deposits cause small changes in the magnetic susceptibility of tissue that measurably affect the local magnetic field and corresponding phase of the MR signal. The observed field pertubations can be modeled as the convolution of a dipole-like kernel with the spatial susceptibility distribution. In the Fourier domain, the kernel exhibits zeros along a conical surface, making the inverse problem ill-posed [22]. In addition, the field can only be measured in regions where the MR signal is valid (i.e. soft tissue). Furthermore, susceptibility differences between typical brain tissue (which is assumed to have approximately the same susceptibility as water) and iron-rich tissue is more than an order of magnitude less than the susceptibility difference between tissue and air ($\chi_{tissue} - \chi_{air} \approx -9.5$ ppm). As a result, tissue/air boundaries create a background field that obscures the subtle iron-related effects of interest. Nonlocal field effects from the neck and torso, lung

expansion during respiration, and imperfect shimming meant to improve field homogeneity also contribute to the background field and corrupt the iron-related phase effects of interest. Thus, eliminating background fields is critical for accurate susceptibility estimation.

Early approaches to susceptibility mapping allowed susceptibility differences to be inferred from parameters such as relaxation rates or phase. For example, in Susceptibility-Weighted Imaging (SWI), developed by Haacke et al., the observed phase data is high-pass filtered to remove background fields. The filtered phase and magnitude data are then combined to produce a composite image which enhances the susceptibility-related phase constrast [17], [23]. While SWI allows excellent visualization of veins, microhemorrhages, and other structures with underlying susceptibility differences, it provides estimates of phase, rather than quantitative susceptibility estimates. In addition, mean SWI values in iron-rich regions of interest in the brain do not always correlate well with postmortem iron estimates [10].

The Field-Dependent Relaxation Rate Increase (FDRI) [14] is computed from spin-echo EPI acquisitions obtained at two different field strengths (i.e. 1.5 and 3 Tesla). The difference in transverse relaxation rate ($R_2 = 1/T_2$) divided by the difference in field strength gives the FDRI. FDRI has been reported to have a high specificity for ferritin [14], which is responsible for storing the largest fraction of iron in the brain that is not found in hemoglobin or iron-containing enzymes (non-heme iron) [8]. Ferritin has been shown to exert a strong magnetic effect that results in marked T_2 shortening in-vitro [24]–[26] and in-vivo [27], [28]. Previous studies have shown that FDRI correlates well with postmortem iron concentrations in young and elderly subjects [10], [12], but may be impractical for many studies since it requires images to be collected on two separate scanners.

Recently, there has been growing interest in solving the inverse problem to obtain quantitative estimates of magnetic susceptibility from measured fieldmaps. Accurate removal of background fields, however, is a central challenge in quantitative susceptibility mapping (QSM). Removing the background field from the measured fieldmap gives the field due only to local susceptibility sources inside the region of interest, which we refer to as the 'background-corrected' or internal magnetic field (B_i). Similarly, we refer to magnetic field sources outside the region of interest as 'external sources' (i.e. air in the sinuses, tissue in the neck, or the shim system) and the corresponding field as the external magnetic field (B_e). Background fields are typically removed using preprocessing strategies that have shown promising results [19], [23], [29]– [34], but may prevent subsequent QSM algorithms from recovering from imperfections in background field estimation. In section II-B, we discuss existing techniques in more detail and describe an iterative approach to simultaneous background field elimination and susceptibility estimation.

Quantitative susceptibility estimates were first obtained by segmenting objects into regions of homogeneous susceptibility, estimating B_i using kernel-based forward models, and solving for the unknown susceptibility by linear least squares fitting of the estimated field to the background-corrected observed field [35]–[38]. Other approaches to QSM have obtained susceptibility estimates in each voxel using threshold-based k-space division [34], [39], multiple orientation sampling [22] or iterative techniques [12], [40]–[44].

Inversion of the forward model by complex division in k-space results in severe noise amplification and streaking artifacts in the estimated susceptibility map. This is due to values in the kernel that are equal or close to zero near a conical surface in k-space that lies at the magic angle of 54.7° relative to B_0. To address this, [39] stabilize the inversion using a threshold-based deconvolution approach, in which points in the deconvolution kernel, $1/\tilde{K}$, that are greater than a truncation parameter, t, are set equal to the value of t that minimizes artifacts in the estimated susceptibility map. Similarly, [34] uses a threshold-based approach, but sets $1/\tilde{K}$ to zero in regions where the values of K are less than a chosen threshold. These techniques reduce streaking artifacts in the estimated susceptibility maps, but involve a trade-off between the accuracy of estimated susceptibility values and severity of the artifact.

[22] showed that zeros can be effectively eliminated from the kernel (at all locations in k-space except the origin) by acquiring data with the object rotated at three of more angles about an axis perpendicular to B_0. They used optimal sampling orientations of −60°, 0°, and 60° and weighted least squares fitting to obtain accurate susceptibility maps in simulation, phantom and ex-vivo tissue experiments. [34] expanded on this work, by showing that accurate susceptibility maps can be estimated from rotations about two orthogonal axes. These results showed improvement over those obtained using three orientations about a single axis for small to moderate rotations in the range of ±20°. Although they obviate the need for regularization, multiple orientation approaches may be difficult to implement in patient studies, due to the difficulty of head rotation in the scanner, limited scan time, and the need for precise registration post-acquisition.

Other methods have recently been developed to estimate susceptibility from a single fieldmap acquisition using iterative techniques that incorporate prior anatomical information [12], [40]–[44]. This approach was first investigated thoroughly by [40] who incorporated the spatial gradients of the magnitude image into an L2 norm penalty to ensure consistency of edge structure in the estimated susceptibility map. [41] included voxel-based constraints derived from lesion geometry and a 'local solution vector' to account for local field shifts unrelated to the underlying susceptibility distribution (i.e. from chemical shift). [42] used the L2 norm to encourage agreement in spatial frequency structure between the magnitude data and estimated susceptibility distribution and the L1 norm to enforce agreement of a partial differential equation, in which the differential operator was similar in form to the wave equation operator. Using the L1-norm of the estimated susceptibility to promote sparse gradients in the estimated susceptiblity map was investigated thoroughly in the L1-QSM method [12]. This method showed promising results in-vivo, but large variance in susceptibility estimates may reduce its efficacy in detecting group differences. [43], [45] and [44] also incorporate the gradient of the magnitude data into a L1 norm penalty on the estimated susceptibility to encourage sparsity and edge structure consistency. Use of L1 and L2 regularization without strong prior knowledge was investigated by [46], who showed stronger suppression of streaking artifacts and background noise using the L1 norm.

In this work, we develop a new method for quantifying susceptibility by inversion of a perturbation model (QSIP). This approach successfully inverts a spatial formulation of the forward model relating magnetic susceptibility to the observed field and requires only a single acquisition. Applying the Laplacian to the observed field eliminates low frequency

background fields that are solutions to the Laplace equation (i.e. shim fields or fields originating from external susceptibility sources). Using the L1 norm with regularization terms involving sparsity-inducing transforms such as the Gradient or Laplacian has shown promising results [12], [42]–[45], motivating its use in this work. In addition, a tissue/air atlas is used to resolve ambiguity between internal and external susceptibility sources that is inherent in the inversion of kernel-based forward models. The QSIP algorithm is applied to data from a study of normal aging and results are validated against in-vivo FDRI and published postmortem iron measurements. Mean susceptibility values in multiple brain regions are computed to investigate age-dependent differences in iron concentration. Results show improved detection of group differences relative to those previously reported for the same data set [12].

II. Methods

A. Fieldmap Estimation and the Forward Model

Several methods have been developed to estimate the magnetic field induced by susceptibility distributions. These include iterative approaches [47]–[51], a perturbation solution of Maxwell's equations in image space [52], and Fourier-based methods [35], [53], [54]. Here, we briefly review two of these kernel-based forward models: the perturbation solution [52] and the Fourier method in [54], which are used in the atlas-based susceptibility estimation and QSIP algorithm described later in this paper. In the first, assuming B_0 is the main field along the z-direction, a Lorentz sphere corrected perturbation solution of Maxwell's equations in continuous space [52] gives an expression for the estimated fieldmap, B:

$$B = \delta B_0 \left[\frac{\chi_1}{3+\chi_0} - \frac{1}{1+\chi_0} \left(\left(\frac{\partial^2 G}{\partial z^2} \right) * \chi_1 \right) \right] \quad (1)$$

$$= (c_1 \delta_0 - c_2 k) * \chi_1, \quad (2)$$

where $G = -1/(4\pi r)$ is the Green's function of the Laplacian, $r = \sqrt{x^2+y^2+z^2}$, where (x, y, z) is the location where the field is being evaluated and $\chi_0 = 0.4$ ppm is the susceptibility of air. The scaled susceptibility, χ_1, is related to the susceptibility, χ, by the expansion, $\chi = \chi_0 + \delta\chi_1$, where δ is a constant equal to the susceptibility difference between tissue and air ($\delta = -9.5$ ppm for the difference between brain tissue and air). In Eq. 2, δ_0 is the Dirac delta function, $c_1 = (\delta B_0)/(3 + \chi_0)$, $c_2 = (\delta B_0)/(1 + \chi_0)$, and $k = (\partial^2 G)/(\partial z^2)$. Eq. 2 can be written concisely as:

$$B = K_s * \chi_1, \quad (3)$$

where $K_s = c_1 \delta_0 - c_2 k$ is the kernel computed in the spatial domain. When the object and corresponding susceptibility distribution are approximated by discrete voxels, K_s is computed using the voxel-based model described in Appendix A.

The forward model developed by [54] provides a Fourier-based method for estimating the magnetic field induced by a susceptibility distribution. The kernel, $\tilde{K}_f$, is derived in the Fourier domain and used to compute the Fourier transform of the fieldmap, $\tilde{B}$, according to:

$$\tilde{B} = B_0 \left(\frac{1}{3} - \frac{k_z^2}{k_x^2 + k_y^2 + k_z^2} \right) \circ \tilde{\chi} \quad (4)$$

$$= \tilde{K}_f \circ \tilde{\chi}, \quad (5)$$

where $\tilde{K}_f = B_0 \left(\frac{1}{3} - \frac{k^2}{k_x^2 + k_y^2 + k_z^2} \right)$ and $\circ$ denotes Hadamard (element-wise) multiplication. Taking the inverse Fourier transform of Eq. 5 gives the predicted fieldmap in image space [54]:

$$B = K_f * \chi. \quad (6)$$

The equivalence of the spatial and Fourier space formulations of the forward model has previously been discussed in some detail [30], [36], [55].

B. Inversion of the Forward Model and Background Field Elimination

Imperfect shimming and fields from external susceptibility sources confound the field due to local susceptibility sources in the region of interest (i.e. the brain). Accurate susceptibility estimation, however, requires careful modeling and removal of this unknown background field from the measured fieldmap. Current approaches to background field removal rely on forward modeling [30], [32], filtering [23], [33], projection of the observed field onto an external susceptibility distribution using an iterative approach [40], estimation of external dipole distributions using least squares fitting [34] and Laplacian-based techniques [19], [29], [42]. [30] registered CT data from a reference subject to the subject of interest and segmented the CT to produce a subject-specific susceptibility model. The predicted fieldmap was computed from the estimated susceptibility map and applied for distortion correction of echo-planar images (EPI). While this method reduced distortion in EPI data, it may not account well for anatomical differences in all cases, especially in sinus regions. [32] also used forward field calculations to remove background field from air/tissue interfaces. The head, sinuses, and mastoid cavities were segmented by a combination of automatic and manual techniques and susceptibility values were estimated by minimization of the residual phase. The need for manual intervention presents a practical disadvantage of this approach and both [30] and [32] used additional preprocessing techniques to remove inhomogeneity from imperfect shimming.

High-pass filtering techniques [23], [33] are robust methods for removing low frequency background fields, but may also eliminate fields of interest from neuronal tissue. The method proposed by [40] is an optimization approach that searches for the distribution of external susceptibility sources and associated background field that best approximates the observed field. This method is more successful than filtering at removing fields due only to external sources, but it may be under-constrained as it does not enforce agreement with

anatomy outside the brain (i.e. the skull). Similarly, the method developed by [34] estimates the background field by least squares fitting of the observed field to a set of fields produced by external dipoles. This method may be overly constrained, since the number of dipoles is restricted for computational purposes. As a result, additional processing (such as 3D polynomial fitting) is required to account for shim fields, which are difficult to model with a relatively sparse dipole distribution.

Shim coils are typically designed to produce fields based on the first and second order terms of a spherical harmonic expansion of the observed field (which are given in cartesian form by x, y, z, xz, yz, xy, (x^2-y^2), and $z^2-(1/2)(x^2+y^2)$ [56], [57]. Since each term is a solution to the Laplace equation, $\nabla B_z = 0$, shims are effectively eliminated by taking the Laplacian of the observed field. More generally, any static magnetic field generated from sources outside the volume of interest is harmonic and satisfies the Laplace equation [29], [58]. Assuming the spatial distribution of the MR signal phase, $\varphi(x, y, z)$, is a linear function of B_z (i.e. no phase aliasing), the phase from external susceptibility sources (i.e. tissue/air interfaces) also satisfies the Laplace equation, $\nabla \varphi = 0$. As a result, several Laplacian-based methods [19], [29], [42] have been proposed for background field elimination. [19] developed an elegant method that uses the spherical mean value (SMV) property of harmonic functions to eliminate the background field. The accuracy of this method, however, may be reduced if unreliable phase data falls within the spatial extent of the SMV convolution kernel. This includes the perimeter of the brain, which is adjacent to air/bone voxels that lack MR signal, and data sets containing substantial B1 inhomogeneities, which are not harmonic. Although non-harmonic fields can be subtracted prior to applying the SMV, this requires two flow-compensated phase data sets, which may not be available in all cases (i.e. standard single-echo SWI sequences).

Given the large contribution of shim and other harmonic fields to the background field, we apply the Laplacian to the forward model in Eq. 1. Since $\chi_0 << 1$ and B_0 is the main field along the z-direction, the expression for the fieldmap, B, is:

$$B = \delta B_0 \left[\frac{\chi_1}{3} - \left(\frac{\partial^2 G}{\partial z^2} * \chi_1 \right) \right]. \quad (7)$$

The forward model in Eq. 7 consists of a local term $\delta B_0(\chi_1/3)$, and the convolution of χ_1 with the second z-derivitive of $G = -\frac{1}{4\pi r}$, which can be rearranged to give:

$$\frac{B}{\delta B_0} - \frac{\chi_1}{3} = \frac{\partial^2}{\partial z^2} \frac{1}{4\pi r} * \chi_1 \quad (8)$$

$$= -\frac{1}{4\pi r} * -\frac{\partial^2 \chi_1}{\partial z^2}. \quad (9)$$

Using the fact that $-\frac{1}{4\pi r}$ is the Green's function for the Laplacian (which we denote here by), applying the Laplacian to Eq. 9 gives:

$$\Delta \left(\frac{B}{\delta B_0} - \frac{\chi_1}{3} \right) = - \frac{\partial^2 \chi_1}{\partial z^2}. \quad (10)$$

Rearranging Eq. 10 gives:

$$\frac{\Delta B}{\delta B_0} = \frac{\Delta \chi_1}{3} - \frac{\partial^2 \chi_1}{\partial z^2} \quad (11)$$

$$= \frac{1}{3} \left[\frac{\partial^2}{\partial x^2} + \frac{\partial^2}{\partial y^2} - 2\frac{\partial^2}{\partial z^2} \right] \chi_1 \quad (12)$$

This can be written concisely as,

$$f(\chi_1) = 3\Delta B / (\delta B_0) \quad \text{where} \quad f = \frac{\partial^2}{\partial x^2} + \frac{\partial^2}{\partial y^2} - 2\frac{\partial^2}{\partial z^2}. \quad (13)$$

Eq. 13 is a hyperbolic partial differential equation (PDE), where f is similar in form to the wave operator. In [42], Eq. 13 was used with the fieldmap magnitude data to successfully remove background fields and obtain accurate susceptibility estimates in phantom data consisting of homogeneous susceptibility regions. In-vivo QSM methods that rely heavily on agreement between observed and predicted field values using kernel-based forward models [12], [19], [22], [40], [42], however, are inherently limited. They cannot distinguish between fields generated by certain susceptibility distributions inside the region of interest, and identical fields produced by external sources. Susceptibility distributions that are eigenfunctions of K_s in Eq. 3 are one example of this; they include constant and linear functions of space along the z direction. Applying the forward model in Eq. 1 to a χ_1 distribution that increases linearly along z in the region of interest, produces a predicted field, B, that is also a linear function of the z-coordinate. This field could, in principle, be produced by an external source, such as a z-shim. [30] have shown that such fields can also be produced by anatomy outside the brain. They demonstrated that the jaw and neck can produce a frequency offset along z, which is approximately linear in the brain, while the torso may produce a global frequency offset. Therefore, when solving the inverse problem, removing all low frequency fields prior to susceptibility estimation will eliminate the background field, but may also eliminate some fields due to the sources of interest. In contrast, inadequate removal of the background field may result in the estimation of artifactual susceptibility distributions in the region of interest. Incorporating prior anatomical information about external (or internal) susceptibility distributions is one way to address this ambiguity. Operations such as   or K_s also result in information loss due to derivatives or zeros in the kernel. This suggests that additional information such as boundary conditions or priors may be necessary to regularize the inversion.

Probabilistic atlases and CT data have frequently been used to compensate for missing information in MR data [52], [59]– [61]. In [61] it was shown that structural MR images of the head can be segmented into tissue-air susceptibility maps using a tissue-air atlas

constructed from CT data. Voxels in the atlas take continuous values between [0, 1] corresponding to susceptibilities ranging from χ_{air} = 0.4 ppm to $\chi tissue$ = -9.1 ppm and are co-registered with the MNI152T1 template [62]. In this work, the susceptibility atlas was used to obtain an initial estimate of external susceptibility sources and the corresponding background field. First, the MNI152T1 template was registered to the magnitude image of the subject of interest (generated during fieldmap acquisition), using 12 degrees of freedom and normalized correlation ratio as the cost function. The resulting transform was then applied to the susceptibility atlas. The co-registered atlas, χ_A, was used to estimate the susceptibility sources, χ, according to:

$$\chi^* = arg \min_{\chi} |M \circ \left(B - K_f * \left(M^C \circ \chi \right) \right)|_2^2, \quad (14)$$

where M is a binary brain mask, B is the observed fieldmap, K_f is the kernel from Eq. 6, and M^C is the complement of M, thus representing the region outside the brain (including structures such as the sinuses). Although the kernels K_s and K_f are effectively equivalent, implementing Eq. 3 and Eq. 6 in discrete space may introduce some discrepancies between the models due to the single voxel approximation (see Appendix A). Error in the discrete perturbation model (Eq. 19) can be reduced by increasing the image resolution, but this may still pose a problem in the case of smooth fields produced by relatively smooth external χ distributions, as smooth distributions are harder to approximate with discrete voxels. Assuming the background field is largely composed of smooth fields (i.e. from mis-set shims), we use the kernel K_f in Eq. 14 rather than incur the computational expense of using K_s, which would require searching over χ distributions with both high resolution and large field of view (to encompass distant sources). Eq. 14 was solved using standard conjugate gradient techniques where χ was initialized to χ_A and the FOV was expanded to search over a large region of external sources. The convolution in Eq. 14 was implemented using the 3D Fast Fourier Transform (FFT).

Following the atlas-based susceptibility mapping (ASM) in Eq. 14, the estimated background field due to external sources, $B_e = K_f * (M^C \bigcirc \chi^*)$, is then used in the QSIP method:

$$\chi_1^* = arg \min_{\chi_1} \left[\lambda_1 |W \circ \left(\Delta B - \frac{\delta B_0}{3} f\left(\chi_1\right) \right)|_1 + \lambda_2 |M \circ (B - (K_s * \chi_1 + B_e))|_2^2 + \lambda_3 |M^C \circ (\chi_1 + \chi_0/\delta)|_2^2 \right], \quad (15)$$

where B_0 is the main field strength, f is the partial derivative operator from Eq. 13, K_s is the kernel from the perturbation model, δ is the susceptibility difference between brain tissue and air ($\delta = -9.5$ ppm), χ_0 is the susceptibility of air (0.4 ppm), and λ_1, λ_2, and λ_3 are constants [55]. The first term in Eq. 15 penalizes departures from Eq. 13, while removing low order background fields. A weighting factor of $W = | B|$, where $|\cdot|$ denotes the absolute value, was chosen to encourage in areas where local susceptibility differences cause agreement high frequency field pertubations (i.e. near boundaries between iron-rich and normal brain tissue where $| B|$ is large). As these regions are relatively sparse, the L1 norm was chosen as described in [12], [42]. Thresholding W enforces agreement only in regions where $| B|$ is large, and makes the L1 norm more robust to noise in the observed fieldmap.

A threshold of 2σ was chosen where σ is the standard deviation of the signal in a noise region of the magnitude image generated by fieldmap acquisition; voxels in W that fall within 2σ were set to 0. The second term encourages agreement of the predicted field, $K_s * \chi_1$, with an estimate of the background-corrected observed field. Since there are no sparsity-inducing transforms in this term, the L2 norm was chosen to promote estimation of accurate susceptibility values throughout the brain, including regions where internal susceptibility distributions may be relatively smooth. Given the expansion, $\chi = \chi_0 + \delta\chi_1$, the third term controls how easily χ_1 values outside the brain can vary from $-\chi_0/\delta$, which is the value of χ_1 when $\chi = 0$. Variation away from this value corresponds to estimating additional external susceptibility sources beyond those computed in Eq. 14. This allows the initial estimate of the background field, B_e, to be updated in an iterative process, in contrast to sequential algorithms that eliminate it in a preprocessing step. Use of the L2 norm discourages large deviations away from the initial estimate of external sources.

Although Eq. 15 is derived from the forward model in Eq. 1, the voxel-based perturbation model (Appendix A) can be used when applying it to estimate discrete χ_1 distributions. In this case, $\frac{\delta B_0}{3} f(\chi_1) \approx \Delta(K_s * \chi_1)$, where K_s is the kernel from Eq. 19, and Eq. 15 can be re-written:

$$\chi_1^* = arg \min_{\chi_1} \left[\lambda_1 |W \circ (\Delta B - \Delta(K_s * \chi_1))|_1 + \lambda_2 |M \circ (B - (K_s * \chi_1 + B_e))|_2^2 + \lambda_3 |M^C \circ (\chi_1 + \chi_0/\delta)|_2^2 \right]. \quad (16)$$

Eq. 16 was solved using a standard conjugate gradient technique; the required convolution was computed using the 3D FFT and the Laplacian was implemented using finite differences. Given fieldmap units of radians/sec, λ_1 was chosen to be $O(1/\gamma)$, where γ is the gyromagnetic ratio (2.675×10^8 radians/sec/T). For any $\lambda_1, \lambda_2 > 0$, setting $\lambda_3 = 0$ results in severe streaking artifacts in the estimated susceptibility map. To find the optimal value of λ_2, streaking artifacts were first eliminated by setting $\lambda_3 \gg \lambda_1$ (i.e. $\lambda_3 = 1 \times 10^{10}$). A search over $1 \times 10^{-12} < \lambda_2 < 1 \times 10^{-4}$ was performed and the value of λ_2 that optimized the relative contributions of the first and second terms was chosen empirically. For studies in which the susceptibility atlas is an approximation of external susceptibility sources (i.e. human subjects with variable sinus anatomy), the value of λ_3 was decreased to an optimal value at which small changes in external susceptibility sources were possible, while streaking artifacts were effectively eliminated.

Once χ_1^* has been estimated, the final susceptibility map can be computed: $\chi^* = \chi_0 + \delta\chi_1^*$. Results of the QSIP algorithm are validated against known susceptibility distributions in phantom data, postmortem iron estimates reported in [8] and compared to previously reported results obtained for the same subjects using FDRI and L1-QSM [12].

C. QSIP: Phantom Experiments

A cylindrical phantom with known susceptibility distributions was constructed. Magnevist (gadopentetate dimeglu-mine) solutions of 0.5, 1.0, 2.0, and 3.0 mM were placed in cylindrical NMR tubes 10 cm in length and 3.43 mm in diameter. The molar susceptibility of 0.027 cgs units/mol Gd was used for conversion [63], giving susceptibility values of 0.15,

0.31, 0.62, and 0.94 ppm respectively. The four tubes were separated by plastic disks and placed in a plastic cylinder filled with water, which measured 22.5 cm in length by 7.2 cm in diameter.

Imaging was conducted on a 3T Siemens Trio MRI system. The phantom was placed horizontally on the patient table and a 12-channel radiofrequency head coil was used. A 3D gradient-recalled echo (GRE) sequence was used (TE1/TE2=10/20 ms, TR=27 ms, 256x256 in-plane, FOV=128x128 mm, 80 slices, thickness=3 mm, FA=25°) to obtain magnitude and phase data for each echo time, and phase unwrapping was performed using Prelude (Phase Region Expanding Labeler for Unwrapping Discrete Estimates) [64]. Masks of the cylindrical container and each NMR tube were generated by thresholding the first magnitude image, and a mask of all four tubes was computed by summing the individual tube masks. A susceptibility atlas was generated by setting all voxels in the cylindrical container mask to have the susceptibility of water. An initial estimate of the external susceptibility sources and background field was computed following Eq. 14, where M was equal to the binary cylinder mask and its complement, M^C, denoted the region outside the phantom.

Two QSIP experiments were conducted to estimate the unknown susceptibility map. In the first, no prior knowledge of the susceptibility distributions within the phantom was assumed and the relative susceptibility maps were computed following Eq.15, using the binary cylinder mask, M, and its complement, M^C. In the second experiment, the region of interest was limited to voxels of unknown susceptibility: M was a binary mask encompassing the four NMR tubes, and M^C denoted the region outside the tubes. Since inversion of the forward model results in estimates of *relative* susceptibility, a baseline correction of the estimated susceptibility map was computed before comparison to known susceptibility values (see section II-D5).

D. QSIP: Validation and application to a study of normal aging

To evaluate the efficacy of QSIP for quantifying susceptibility in-vivo, we applied our method to the data set of young and elderly subjects first described in [10]. Results are compared to previous studies that examined the performance of FDRI [10] and L1-QSM [12]. In L1-QSM, background fields were eliminated by projecting the observed field onto an external susceptibility distribution as described by [31]. Here we analyze the same data set used in previous L1-QSM and FDRI studies [10], [12], which is summarized below.

1) Subjects—Two groups of healthy, highly educated, right-handed adults were studied: 11 younger adults (mean ± S.D. age=24.0±2.5, range=21 to 29 years, 15.9 years of education; 5 men, 6 women) and 12 elderly adults (mean±S.D. age=74.4±7.6, range=64 to 86 years, 16.3 years of education; 6 men, 6 women). The younger subjects included laboratory members and volunteers recruited from the local community. All older participants were recruited from a larger ongoing study of normal aging and scored well within the normal range on the Dementia Rating Scale [65]: mean=140.6, range=132 to 144 out of 144, cut-off for dementia=124. Mean (and range) of days between 1.5 T and 3.0 T scan acquisition were 16.5 (0 to 56) days for the young and 9.3 (0 to 42) days for the elderly

group; for 2 of the young and 8 of the elderly both sets of scans were acquired on the same day.

2) Image acquisition protocols—MRI data were acquired prospectively on 1.5 T and 3.0 T General Electric (Milwaukee, WI) Signa human MRI scanners (gradient strength=40 mT/m; slew rate=150 T/m/s).

<u>**FDRI acquisition:**</u> At 1.5 T, after auto shimming for the session, the following sequences were acquired:

1)   3D Spoiled Gradient Recalled Echo (SPGR) for structural imaging and registration (TR/TE=8.1/3.3 ms, FA=30°, 512×256 in-plane, FOV=24 cm, 62 slices, 2.5 mm thick);

2)   multi-shot Echo Planar Spin Echo (EPSE) (TR/TE=6000/17 ms, FA=90°, 256×192 in-plane, FOV=24 cm, 4 NEX, 24 interleaves with 8 phase-encode lines per TR, 62 slices, 2.5 mm thick, 9:40 min);

3)   multi-shot EPSE (TR/TE=6000/60 ms, FA=90°, 256×192 in-plane, FOV=24 cm, 6 NEX, 24 interleaves, 62 slices, 2.5 mm thick, 14:20 min).

At 3.0 T, after auto shimming for the session, the following sequences were acquired in the axial plane:

1)   3D SPGR for structural imaging and registration (TR/TE=8.1/3.3 ms, FA=15°, 256×256 in-plane, FOV=24 cm, 124 slices, 1.25 mm thick);

2)   multi-shot EPSE (TR/TE=6000/17 ms, FA=90°, 256×192 in-plane, FOV=24 cm, 3 NEX, 24 interleaves, 62 slices, 2.5 mm thick, 7:10 min);

3)   multi-shot EPSE (TR/TE=6000/60 ms, FA=90°, 256×192 in-plane, FOV=24 cm, 6 NEX, 24 interleaves, 62 slices, 2.5 mm thick, 14:20 min).

<u>**Susceptibility-weighted image acquisition:**</u> In practice, 'susceptibility-weighted imaging' (SWI) is often used to refer to both a type of MRI acquisition and a method for analyzing the data collected from gradient-echo sequences [17], [23]. Gradient-echo sequences generate magnitude and phase data, which are suitable for further SWI analysis, or the phase maps may be used as inputs to QSM algorithms, such as the QSIP method described in this article. At 1.5 T, after auto shimming for the session, the following sequences were acquired for 62 axial slices, each 2.5 mm thick:

1)   3D SPGR for structural imaging and registration (TR/TE=28/10 ms, FA=30°, 256×256 in-plane, 24 cm FOV);

2)   Susceptibility-weighted 3D SPGR (TR/TE=58/40 ms, FA=15°, 512×256 in-plane, 24 cm FOV, 12:20 min, with flow compensation) [9], [17];

Phase images were constructed from the real and imaginary components of the susceptibility-weighted SPGR data after phase unwrapping with FSL PRELUDE [64]. The magnitude and phase-unwrapped SWI data were down-sampled from 512×256 to 256×256 via averaging to match the FDRI resolution. Brain masks were generated with the FSL Brain

Extraction Tool, BET [66]. After estimating the fieldmaps from the unwrapped phase data with the down-sampled size 256×256, relative susceptibility maps were computed with the QSIP algorithm.

3) Image Registration—The image registrations were performed as described previously [10], [12] and are summarized here. The late-echo EPSE data were non-rigidly registered [67] [http://www.nitrc.org/projects/cmtk/] to the early-echo EPSE data for each subject and each field strength. The 1.5 T early-echo EPSE image of each subject was registered to the 3.0 T early-echo EPSE image of the same subject, which was then registered non-rigidly to the subject's 3.0 T SPGR image. Following brain extraction with BET, the 3.0 T SPGR image from each subject, was registered non-rigidly to the SPGR channel of the SRI24 atlas [68] [http://www.nitrc.org/projects/sri24/]. Calculated transformations were concatenated and applied to reformat all EPSE images into 1-mm isotropic SRI24 space. The 1.5 T SWI magnitude images were rigidly registered to the corresponding structural SPGR image, which was then registered non-rigidly to the same subject's 3.0 T SPGR image. Transformations were then concatenated and applied to reformat the SWI phase images and QSIP results (which were computed in native space) to 1-mm isotropic SRI24 space for the purpose of computing group averages. For the QSIP results, separate young and elderly group averages were computed for visualization purposes only.

4) Calculation of group averages and region-of-interest (ROI) identification and analysis—For each subject and for each ROI at each field strength, the mean intensity of all voxels in an ROI for the early- and late-echo EPSE were used to compute $R2_{3T}$ and $R2_{1.5T}$. FDRI images (FDRI = $(R2_{3T}-R2_{1.5T})/1.5$ T) were computed [10], [14], [69] for each subject and used to make a group FDRI average, comprising all young and elderly subjects. A similar group average was made for the phase data. The FDRI and phase averages were used to guide ROI delineation as described below. Separate young and elderly group averages of the FDRI data were also computed for visualization purposes.

As previously described [10], bilateral caudate, globus pallidus, putamen, thalamus, and white matter sample regions of interest (ROIs) were drawn (by A.P.) on the group-average (all young plus all elderly subjects) FDRI images in common SRI24 space, reformatted in the *coronal* plane. The globus pallidus, putamen, caudate, and white matter sample were drawn on 10 contiguous, 1-mm thick slices at an anterior -posterior location that maximized the presence of all three basal ganglia structures in the same slices. The thalamus was drawn on the next 10 contiguous slices posterior to the basal ganglia. The caudate was eroded one pixel and thalamus was eroded two pixels on a slice-by-slice basis to avoid partial voluming of CSF. Substantia nigra and red nucleus ROIs were also identified based on their FDRI intensities. The same ROIs were also manually identified on the group-average phase data (all young and all elderly subjects combined), reformatted in the *axial* plane [70], and guided by phase conspicuity. When drawing ROIs on the phase data, an effort was made to exclude the bright rims around the globus pallidus and putamen as well as the division between them. Although this approach biases the data towards more negative phase (i.e., lower values reflecting less iron), its purpose was to maximize the sensitivity of phase to age

effects. Thus, iron estimates were conducted on both sets of ROI identifications, the phase-guided and the FDRI-guided.

For each subject, the mean $R2_{3T}$, $R2_{1.5T}$, and FDRI were computed for each ROI from the early- and late-echo EPSE data. All QSIP results were computed in the native space of each subject and the ROIs were projected onto each subject's QSIP data. Mean relative magnetic susceptibility in parts per million (ppm) in each ROI were computed from each subject's QSIP results. ROI averages were computed twice following both FDRI-guided (*axial*) and phase-guided (*coronal*) ROI delineation.

5) Baseline correction of estimated susceptibility values—The estimated susceptibility map is inherently a distribution of relative susceptibility values. As described in Appendix B, susceptibility may be defined with respect to a reference value (i.e. susceptibility of air), but this (or any other) reference is effectively eliminated by setting the kernel to zero at the k-space origin. For meaningful interpretation of QSM results, it is necessary to establish some new reference and report susceptibility values relative to it. In [12], the average susceptibility in the splenium of each subject was used as the reference for baseline correction of the subject's L1-QSM results. We took the same approach in this work, and used the mean splenium susceptibility in each subject for correction of the QSIP results, producing baseline corrected susceptibility estimates (QSIP-C). As described in [12], the splenium was preferred over taking CSF as a reference since the susceptibilities were observed to differ substantially between anterior and posterior regions of the ventricles in this data set. The mean splenium susceptibility in the young and elderly groups did not differ significantly, but was slightly larger in the elderly group $\left(\chi_{splenium}^{Elderly} = -.0345 \quad ppm\right)$ than the young group $\left(\chi_{splenium}^{Young} = -.0352 \quad ppm\right)$. This is similar to mean values previously reported using the L1-QSM method $\left(\chi_{splenium}^{Elderly} = -.0378 \quad ppm\right)$ and $\left(\chi_{splenium}^{Young} = -.0479 \quad ppm\right)$ [12]. In both cases, this should introduce a small bias against observing higher susceptibility values in young relative to elderly groups. More importantly, the use of such a reference may increase the variance of baseline-corrected susceptibility values (relative to the uncorrected values), which could reduce the statistical power of group differences. This could occur, for example, if the elimination of background fields in the splenium was not consistent across subjects, resulting in artifactually greater variance of splenium susceptibility, which would then propagate to the baseline-corrected susceptibility values. To account for this possibility, all subsequent analysis was carried out on both corrected ('QSIP-C') and uncorrected ('QSIP') results.

6) Statistical analysis—We hypothesized that average susceptibility values in each ROI obtained with QSIP and QSIPC would correlate positively with published postmortem iron [8] and FDRI values [10]. Validation of our results against postmortem values and FDRI were based on nonparametric Spearman correlations. In addition, we compared our correlations to published results of the L1-QSM method [12]. Statistical significance of correlation coefficient differences across methods was assessed using the Fisher transformation. We then tested the hypotheses that the elderly group would have higher

QSIP and QSIP-C values in striatal and brain stem ROIs, but not in thalamic or white matter ROIs. To assess group differences, p-values were calculated using two-tailed t-tests with $a = 0.05$. Directional hypotheses regarding group differences were considered significant for p 0.0125, the corresponding one-tailed, family-wise Bonferroni-corrected p-value for 8 measures. All analysis was conducted using both FDRI-guided and phase-guided ROIs.

III. Results

A. Comparison of QSIP with known susceptibility values: results of the phantom experiments

Results of the phantom experiments are shown in Fig. 1. Magnitude and fieldmap images computed from the MR signal are shown in rows 1 and 2 of Fig. 1a, respectively. The magnitude image shows homogeneous contrast across the four tubes, while the fieldmap intensities increase as a function of gadolinium concentration. The fieldmap shows substantial background fields from external sources (i.e. air and shim), which are successfully eliminated by applying the Laplacian (Fig. 1a, row 3). In the QSIP analysis, parameters for each term were optimized as described in section II-B, giving $\lambda_1 = $ 1e-8, $\lambda_2 = $ 1e-6, and $\lambda_3 = $ 1e10. Baseline correction of QSIP results was applied as described in section II-C to obtain QSIPC susceptibility estimates.

QSIP-C results show strong agreement with ground truth susceptibility values (Fig. 1b). A plot of estimated versus true susceptibility for the four tubes gives a slope of 1.06 for experiment 1 and 0.98 for experiment 2. The increase in susceptibility as a function of gadolinium concentration can be seen in axial cross-sections in row 2, for both experiment 1 (column 1) and experiment 2 (column 2).

B. Correlations of QSIP with postmortem iron concentrations

Young and elderly group averages from the QSIP results are shown adjacent to the corresponding FDRI group averages in Fig. 2. The QSIP results show an age-dependent increase in estimated susceptibility values in sub-cortical regions known to accumulate iron in normal aging. Fig. 3 shows the mean±SD iron concentration in each ROI [8] on the x-axis and the mean±SD FDRI values in s^{-1}/T, as well as the L1-QSM and QSIP-C values in ppm on the y-axis for both elderly and young subjects. In the elderly subjects, the correlations between QSIP-C and postmortem data are high (Rho=0.905, p=0.0023) and agree well with published results for FDRI (Rho=0.952, p=0.0006) and L1-QSM (Rho=0.905, p=0.0023) computed on the same subjects [12]. No statistically significant difference in the correlation coefficients (Rho=0.905 and Rho=0.952) was observed (z=0.75, p=0.45, two-tailed). In the young subjects, QSIP-C shows strong correlation with postmortem measurements (Rho=0.976, p=0.0002), which is an improvement over L1-QSM (Rho=0.762, p=0.0184), and this difference in Rho is statistically significant (z=2.41, p=0.016, two-tailed). The QSIP-C correlation with postmortem data in young subjects is comparable to FDRI (Rho=0.976, p=0.0002); no difference in the correlation coefficients is observed between these methods.

C. Correlations between QSIP and FDRI

Fig. 4 shows the correlations between FDRI and L1-QSM, QSIP-C, and QSIP in both elderly and young subjects. In the elderly subjects, QSIP results correlate highly with the FDRI (*Rho*=0.952, *p*=0.0006), consistent with published L1-QSM correlations (*Rho*=0.952, *p*=0.0006), and no difference in correlation coefficients is observed. In the young subjects, QSIP shows excellent agreement with FDRI (*Rho*=1.00, *p*=0.00002) and improvement over L1-QSM (*Rho*=0.857, *p*=0.0054); this difference in *Rho* is statistically significant (*z*=5.04, *p*=0, two-tailed). In the young subjects, the QSIP plots show reduced variance in 5 of 8 ROIs relative to the L1-QSM results and in 7 of 8 ROIs relative to the QSIP-C results. In the elderly subjects, the QSIP plots show reduced variance in 7 of 8 ROIs relative to the L1-QSM results and in all ROIs relative to the QSIP-C results.

D. Group differences in regional iron concentration identified with QSIP

Since previous statistical analysis of this data set showed no consistent cerebral hemisphere asymmetries across iron-rich structures [10], statistical analysis of group differences was computed on bilateral data (computed as the mean of the left and right measurements for each ROI). Results of the statistical analysis are shown in Fig. 5. The QSIP-C results are consistent with L1-QSM results, showing greater iron concentration in the elderly subjects in the putamen, substantia nigra, red nucleus, and globus pallidus. Results of the QSIP algorithm without baseline correction are similar to those of QSIP-C, but results of QSIP show smaller *p*-values due to reduced variance. All *t*-test and *p*-values are presented in Tables 1-4 of the supplemental material for both FDRI- and phase-guided ROIs.

IV. Discussion

In this work, we presented a new method for quantifying susceptibility by inversion of a perturbation model in the spatial domain. QSIP demonstrated the ability to detect group differences in iron concentration between young and elderly subjects in regional striatal and brain stem nuclei, and showed greater differences and improved statistical significance relative to L1-QSM results reported for the same data. QSIP results from both FDRI-guided and phase-guided ROIs were validated against postmortem and FDRI iron measurements. Correlations between QSIP and postmortem data were high in both young and elderly subjects and agreed well with correlations previously reported between FDRI and postmortem iron concentrations. Further validation was obtained by directly comparing in vivo results (QSIP and FDRI), which showed strong correlation. Third, validation was provided by computing age-related group differences in QSIP values; higher iron concentrations in elderly adults were observed in striatal and brain stem nuclei (caudate nucleus, putamen, globus pallidus, red nucleus, and substantia nigra), consistent with FDRI. Finally, QSIP results both before and after baseline correction were compared to previously reported L1-QSM susceptibility estimates. Correlations of QSIP with postmortem data in elderly subjects are equal or greater than those obtained with L1-QSM for FDRI-guided and phase-guided ROIs, respectively. In young subjects, correlations of QSIP with postmortem data are higher than L1-QSM in FDRI-guided and phase-guided results. Similarly, comparable or better correlations of QSIP with in-vivo FDRI were observed relative to L1-QSM. In the group difference results, L1-QSM showed statistically significant increases in

QSM values in four striatal and brain stem nuclei (putamen, globus pallidus, red nucleus, and substantia nigra) across FDRI-guided or phase-guided analysis. FDRI results from both FDRI-guided and phase-guided ROIs showed a statistically significant difference in only one of these structures (putamen), while QSIP showed significant differences in all five (caudate nucleus, putamen, substantia nigra, red nucleus, and globus pallidus). In addition, QSIP did *not* show a significant increase in QSM values in frontal white matter, dentate nucleus, or thalamus. These results are consistent with the hypothesis of age-dependent iron accumulation in striatal and brain stem nuclei. The increase in statistically significant results using QSIP can be attributed to the reduced variance in mean susceptibility estimates. This is important since reduced variance would provide greater statistical power in future clinical studies that seek to investigate group differences in iron concentration between patients and controls. For example, it has been hypothesized that iron accumulation in the substantia nigra (SN) may be a sub-clinical marker of Parkinson's Disease [72], but this has yet to be confirmed with existing QSM methods. [73] computed susceptibility maps for a volume of tissue encompassing the SN of Parkinson's patients, using 7 Tesla data and a threshold-based k-space approach. Although they showed an increase in susceptibility of the SN in Parkinson's patients, group differences were not statistically significant after controlling for age.

In this work, we analyzed both phase-guided and FDRI-guided ROIs, and applied baseline correction of QSIP susceptibility estimates using splenium as a reference, to be consistent with previous analysis of this data set [12]. Similar to the results in [12], the mean susceptibility value in the globus pallidus using the QSIP-C method (0.10–0.13 ppm, splenium reference) is slightly lower than values previously reported for young subjects (approximately 0.20 ppm, with CSF as reference) [19], [74], which is likely due to inter-subject averaging and partial volume effects arising from the 2.5 mm slice thickness as described in [12]. While baseline correction yields absolute susceptibility values in reasonable agreement with previously published QSM estimates, the correction does not affect correlations with postmortem iron concentrations or FDRI. Relative susceptibility differences between groups, however, are likely to be of greater interest in clinical studies. In this case, QSIP produces favorable results. The reduced variance in uncorrected susceptibility estimates may be due to inherent variability in splenium susceptibility, to anisotropic susceptibility effects that have been reported in white matter [75], or to less robust background field elimination in this region. While several studies have shown diamagnetic susceptibility values for myelin [19], [33], its magnetic properties and relative contribution to phase contrast is an area of active research. Since lipid concentration is known to be much lower in gray matter than in white matter [76], and substantial age-dependent iron accumulation has been shown in postmortem analysis [8], we have implicitly assumed any potential myelin-based susceptibility differences between groups are negligible in the gray matter structures we examined. It is possible, however, that if such differences exist, they would confound inferences about iron concentration, especially at higher field strengths, or in regions where exclusion of adjacent white matter voxels by manual segmentation is more difficult. More accurate data regarding the relative contribution of myelin and non-heme iron to voxel-based susceptibility estimates is necessary to advance the interpretation and application of future QSM studies.

Other factors that contribute to uncertainty in QSM results include discrete sampling of the continuous Green's function and continuous susceptibility distribution, low signal-to-noise ratio (SNR), and errors associated with manual delineation of ROIs. Discretization of the kernel results in uncertainty in susceptibility estimates that is inherent in all QSM methods and has been discussed in some detail in [36], [54] and [30]. Voxels with low SNR (i.e. due to signal loss or partial volume effects) may reduce the accuracy of QSM estimates, but substantial signal loss was not observed in the 1.5 T data set used in this study. At higher field strengths these voxels can be identified from two fully flow-compensated data sets and excluded from analysis as described by [19]. Uncertainty due to voxel-based approximation of the susceptibility distribution can be reduced by acquiring data with high spatial resolution. The relatively small diameter of the cylindrical ROIs used in the phantom study, however, may have resulted in imperfection in ROI boundaries and account for some of the error in estimated susceptibility values. The impact of any errors in ROI delineation in the human study was reduced by analyzing data from both FDRI-guided and phase-guided ROIs. A noticeable difference, however, was seen between phase-guided and FDRI-guided results in elderly subjects in the globus pallidus across all methods (QSIP, L1-QSM, and FDRI). This may be due to reduced SNR in this region, leading to error in ROI delineation; in phase-guided striatal nuclei, the globus pallidus had the lowest SNR on average across all subjects (7:1).

While other QSM methods such as L1-regularized QSM [12] have performed well in-vivo, QSIP also shows strong results, and provides additional methodological contributions. First, the background field removal technique developed in [31] and applied in [12] is further developed here, by incorporating a tissue/air susceptibility atlas. The atlas is useful in segmenting air from bone, and for this purpose affine registration of the atlas was found, empirically, to provide good results. The use of affine transforms also potentially increases robustness from using fewer parameters than nonlinear registration. The co-registered atlas, however, provides only an estimate of true anatomy, and therefore is used only to provide a more anatomically meaningful initialization of susceptibility outside the brain. The initial atlas-based estimate is updated iteratively when solving Eq. 14, and sources outside the brain can be further optimized when solving Eq. 15 by varying the strength of λ_3. Second, the QSIP method does not enforce agreement between edges in the magnitude data and estimated susceptibility map, which may be advantageous in certain pathologies. Third, to our knowledge this is the first work to investigate inversion of the spatial formulation of the forward model described in [52] for the purpose of computing whole brain susceptibility maps. Finally, this work builds on the innovative development of susceptibility-weighted imaging (SWI) by [9], [17], [23]. While the high-pass filtering approach used in SWI is highly effective at removing low-order background fields, it may also remove phase effects due to internal susceptibility sources, which may confound the final SWI results. The phase data from SWI acquisitions, however, can also be used as input to a variety of QSM algorithms, such as the one described in this article, to obtain quantitative susceptibility maps. The increasingly widespread adoption of SWI is thus a great asset for this work, as QSIP could be used for retrospective analysis of SWI studies to provide complementary quantitative estimates of tissue susceptibility.

V. Conclusion

We presented a quantitative susceptibility mapping algorithm that inverts a spatial formulation of the forward model and incorporates a tissue/air susceptibility atlas to quantify susceptibility in-vivo. An important limitation of the validation presented herein is the lack of direct comparisons to other QSM results using a single phantom data set. Such experiments are impeded by a lack of standardized data sets and open-source implementations of existing QSM techniques. Detailed comparisons of QSIP to L1-QSM were provided for the same human data, however, in addition to correlations of QSIP with both FDRI and postmortem iron. The QSIP method demonstrated favorable results relative to currently published QSM algorithms, including stronger correlations with FDRI and postmortem iron measurements and reduced variance in mean susceptibility estimates in multiple brain regions. Results from a study of normal aging suggest QSIP could provide valuable insight into the pathophysiology of iron deposition known to occur in neurodegenerative disease [1]– [7]. In comparison to other QSM algorithms and susceptibility-related techniques, QSIP provides accurate susceptibilty maps from data acquired at a single field strength without the need for patient re-positioning or strong agreement with observed magnitude data. The reduced variance in susceptibility estimates may also provide increased statistical power for detecting group differences. Thus, QSIP has demonstrated the potential to be a valuable tool for future clinical studies of neurodegenerative disorders.

Acknowledgments

Appendix A

Discretization of the Perturbation Model

The perturbation model in Eq. 1 requires the susceptibility distribution to be specified at each point in space, making the convolution analytically intractable for complicated functions. Approximating the object and corresponding susceptibility distribution by discrete voxels, however, allows the convolution in Eq. 1 to be calculated analytically for a single voxel with $\chi_1 = 1$ [52]:

$$
\begin{aligned}
H\left(x, y, z\right) &= \int \int \int_{voxel} \frac{\partial^2 G}{\partial z^2}\left(x, y, z\right) dx \quad dy \quad dz \\
&= \frac{1}{4\pi} tan^{-1}\left(\frac{xy}{zr}\right).
\end{aligned}
\tag{17}
$$

Due to the linearity of Eq. 1, the single voxel solutions can be added together to give the final fieldmap:

$$
B = \left(c_1 \delta_0 - c_2 H\right) * \chi_1 \tag{18}
$$

$$
B = K_s * \chi_1, \tag{19}
$$

where $K_s = c_1 \delta_0 - c_2 H$ is the discrete kernel in the spatial domain. The single voxel solution, H, replaces k in Eq. 2, and δ_0 is the Kronecker delta function.

Appendix B

Equivalence of the Forward Models

[30] and [36] have previously shown that the forward model is equivalent in the Fourier and spatial domains. Here, we show that this equivalence holds for the spatial formulation in Eq. 1 under the condition that $\chi_0 = 0$. Taking the Fourier transform of Eq. 1 gives:

$$\tilde{B} = \delta B_z^{(0)} \left[\frac{1}{3+\chi_0} - \frac{1}{1+\chi_0} \left(\frac{k_z^2}{k_x^2+k_y^2+k_z^2} \right) \right] \circ \tilde{\chi}_1 \quad (20)$$

where the Fourier transform of χ_1 is given by $\tilde{X}_1 = \frac{1}{\delta} \left(\tilde{\chi} - \chi_0 \delta_0 \right)$. Eq. 20 can then be re-written as:

$$\begin{aligned} \tilde{B} = \ & B_z^{(0)} \left[\frac{1}{3+\chi_0} - \frac{1}{1+\chi_0} \left(\frac{k_z^2}{k_x^2+k_y^2+k_z^2} \right) \right] \circ \tilde{\chi} - \\ & B_z^{(0)} \left[\frac{1}{3+\chi_0} - \frac{1}{1+\chi_0} \left(\frac{k_z^2}{k_x^2+k_y^2+k_z^2} \right) \right] \circ \delta_0 \chi_0 \end{aligned} \quad (21)$$

The second term arises from the fact that the forward model in Eq. 1 defines all measurements with respect to vacuum, requiring an offset of $\chi_0 = 0.4$ ppm. Susceptibility values are typically quoted with respect to vacuum, but the fields of interest will generally be measured in air. The forward model can be formulated with respect to air as a reference (for both fields and susceptibility) or with respect to vacuum. In Eq. 1, the latter is done and so a constant offset for all fields is required, whereas if it is formulated with respect to air, no offset is necessary as long as the susceptibility is also provided as a difference with respect to air.

The value of the kernel at the k-space origin determines the effect of the second term on the model, and so requires careful consideration. The magnetic induction at the origin is equal to the Lorentz sphere term (the second term in equation (5.64) in [77]). Given this, [36] have noted that comparison of the forward model (see equation (1) in [36], equation (3) in [54] or equation (5.56) in [77]) with the expression for the magnetic induction (equation (5.64) in [77]), shows that it is consistent to set $\tilde{B} = 0$ at $k = 0$. Setting the kernel to zero at the k-space origin eliminates the second term in Eq. 21. Then, for $k \neq 0$,

$$\tilde{B} = B_z^{(0)} \left[\frac{1}{3+\chi_0} - \frac{1}{1+\chi_0} \left(\frac{k_z^2}{k_x^2+k_y^2+k_z^2} \right) \right] \circ \tilde{\chi}, \quad (22)$$

and the Fourier and spatial models are effectively equivalent since $\chi_0 << 1$. Alternatively, one can set $\chi_0 = 0$. Doing this assumes susceptibility and magnetic field values are measured with respect to air. The two models are then equivalent for all k, and the value of the kernel at the k-space origin is set to zero as previously described.

REFERENCES

1. Zecca L, Youdim M, Riederer P, Connor J, Crichton R. Iron, brain ageing and neurodegenerative disorders. Nat Rev Neurosci. Nov.2004 5:863–73. [PubMed: 15496864]

2. McNeill A, Chinnery P. Neurodegeneration with brain iron accumulation. Handb Clin Neurol. 2011; 100:161–72. [PubMed: 21496576]

3. Kurian M, McNeill A, Lin J, Maher E. Childhood disorders of neurodegeneration with brain iron accumulation (NBIA). Dev Med Child Neurol. 2011; 53(5):394–404. [PubMed: 21480873]

4. Lassmann H. Mechanisms of neurodegeneration shared between multiple sclerosis and alzheimer's disease. J Neural Transm. 2011; 118(5):747–52. [PubMed: 21373761]

5. Jellinger K, Paulus W, Grundke-Iqbal I, Riederer P, Youdim M. Brain iron and ferritin in parkinson's and alzheimer's diseases. J Neural Transm Park Dis Dement Sect. 1990; 2(4):327–40. [PubMed: 2078310]

6. Perry G, Sayre L, Atwood C, Castellani R, Cash A, Rottkamp C, Smith M. The role of iron and copper in the aetiology of neurodegenerative disorders: therapeutic implications. CNS Drugs. 2002; 16(5):33952.

7. Bartzokis G, Lu P, Tishler T, Fong S, Oluwadara B, Finn J, Huang D, Bordelon Y, Mintz J, Perlman S. Myelin breakdown and iron changes in huntington's disease: pathogenesis and treatment implications. Neurochem Res. 2007; 32(10):1655–64. [PubMed: 17484051]

8. Hallgren B, Sourander P. The effect of age on the non-haemin iron in the human brain. J Neurochemistry. 1958; 3:41–51.

9. Haacke E, Ayaz M, Khan A, Manova E, Krishnamurthy B, Gollapalli L, Ciulla C, Petersen IKI,F, Kirsch W. Establishing a baseline phase behavior in magnetic resonance imaging to determine normal vs. abnormal iron content in the brain. J Magn Reson Imaging. Aug.2007 26:256–64. [PubMed: 17654738]

10. Pfefferbaum A, Adalsteinsson E, Rohlfing T, Sullivan E. MRI estimates of brain iron concentration in normal aging: comparison of field-dependent (FDRI) and phase (SWI) methods. Neuroimage. Aug.2009 47:493–500. [PubMed: 19442747]

11. Raz N, Rodrigue K, Haacke E. Brain aging and its modifiers: insights from in-vivo neuromorphometry and susceptibility weighted imaging. Ann N Y Acad Sci. Feb.2010 1097:84–93. [PubMed: 17413014]

12. Bilgic B, Pfefferbaum A, Rohlfing T, Sullivan E, Adalsteinsson E. MRI estimates of brain iron concentration in normal aging using quantitative susceptibility mapping. Neuroimage, Sep. 2011

13. Koeppen A. The history of iron in the brain. J Neurol Sci. 1995; 134:1–9. [PubMed: 8847538]

14. Bartzokis G, Aravagiri M, Oldendorf W, Mintz J, Marder S. Field dependent transverse relaxation rate increase may be a specific measure of tissue iron stores. Magn Reson Med. 1993; 29(4):459–64. [PubMed: 8464361]

15. Bartzokis G, Sultzer D, Mintz J, Holt L, Marx P, Phelan C, Marder S. In-vivo evaluation of brain iron in alzheimer's disease and normal subjects using MRI. Biol Psychiatry. Apr; 1994 35(7):480–7. [PubMed: 8018799]

16. Bartzokis G, Beckson M, Hance D, Marx P, Foster J, Marder S. MR evaluation of age-related increase of brain iron in young adult and older normal males. Magn Reson Imaging. 1997; 15(1):29–35. [PubMed: 9084022]

17. Haacke E, Cheng N, House M, Liu Q, Neelavalli J, Ogg R, Khan A, Ayaz M, Kirsch W, Obenaus A. Imaging iron stores in the brain using magnetic resonance imaging. Magn Reson Med. Jan.2005 23:1–25.

18. Yao B, Li T, Gelderen P, Shmueli K, de Zwart J, Duyn J. Susceptibility contrast in high field mri of human brain as a function of tissue iron content. Neuroimage. Feb.2009 44:1259–66. [PubMed: 19027861]

19. Schweser F, Deistung A, Lehr B, Reichenbach J. Quantitative imaging of intrinsic magnetic tissue properties using MRI signal phase: an approach to invivo brain iron metabolism. Neuroimage. Feb.2011 54:2789–807. [PubMed: 21040794]

20. Berg D. In-vivo detection of iron and neuromelanin by transcranial sonography–a new approach for early detection of substantia nigra damage. J Neural Transm. Jun; 2006 113(6):775–80. [PubMed: 16755382]

21. Zecca L, Berg D, Arzberger T, Ruprecht P, Rausch W, Musicco M, Tampellini D, Riederer P, Gerlach M, Becker G. In-vivo detection of iron and neuromelanin by transcranial sonography: a new approach for early detection of substantia nigra damage. Mov Disord. Oct; 2005 20(10): 1278–85. [PubMed: 15986424]

22. Liu T, Spincemaille P, de Rochefort L, Kressler B, Wang Y. Calculation of susceptibility through multiple orientation sampling (COSMOS): a method for conditioning the inverse problem from measured magnetic field map to susceptibility source image in MRI. Magn Reson Med. Jan.2009 61:196–204. [PubMed: 19097205]

23. Haacke E, Xu Y, Cheng Y, Reichenbach J. Susceptibility weighted imaging (SWI). Magn Reson Med. Sep.2004 52:612–8. [PubMed: 15334582]

24. Koenig S, Baglin C, R. B. Magnetic field dependence of solvent proton relaxation in aqueous solutions of Fe3+ complexes. Magn Reson Med. Jun; 1985 2(3):283–8. [PubMed: 3938511]

25. Koenig S, R. B. Gibson J, Ward R, Peters T. Relaxometry of ferritin solutions and the influence of the Fe3+ core ions. Magn Reson Med. Oct.1986 3(5):755–67. [PubMed: 3784891]

26. Gillis SKP. Transverse relaxation of solvent protons induced by magnetized spheres: application to ferritin, erythrocytes, and magnetite. Magn Reson Med. Oct.1987 5(4):323–45. [PubMed: 2824967]

27. Thulborn K, Sorensen A, Kowall N, McKee A, Lai A, McKinstry R, Moore J, Rosen B, Brady T. The role of ferritin and hemosiderin in the MR appearance of cerebral hemorrhage: a histopathologic biochemical study in rats. Am J Neuroradiol. 1990; 11(2):291–7. [PubMed: 1690500]

28. Brittenham G, Farrell D, Harris J, Feldman E, Danish E, Muir W, Tripp J, Bellon E. Magnetic-susceptibility measurement of human iron stores. N Engl J Med. Dec.1982 307(27):1671–5. [PubMed: 7144866]

29. Li L, Leigh J. High-precision mapping of the magnetic field utilizing the harmonic function mean value property. J Magn Reson. Feb.2001 148:442–8. [PubMed: 11237651]

30. Koch K, Papademetris X, Rothman D, de Graaf R. Rapid calculations of susceptibility-induced magnetostatic field perturbations for in-vivo magnetic resonance. Phys Med Biol. 2006; 51(24): 6381–6402. [PubMed: 17148824]

31. Liu T, Khalidov I, de Rochefort L, Spincemaille P, Liu J, Tsiouris A, Wang Y. A novel background field removal method for MRI using projection onto dipole fields (PDF). NMR Biomed. 2011; 24(9):1129–36. [PubMed: 21387445]

32. Neelavalli J, Cheng Y, Jiang J, Haacke E. Removing background phase variations in susceptibility-weighted imaging using a fast, forward-field calculation. J Magn Reson Imaging. Apr; 2009 29(4): 937–48. [PubMed: 19306433]

33. Duyn J, van Gelderen P, Li T, de Zwart J, Koretsky A, Fukunaga M. High-field MRI of brain cortical substructure based on signal phase. Proc. Natl. Acad. Sci. 2007; 104:1179611801.

34. Wharton S, Schfer A, Bowtell R. Susceptibility mapping in the human brain using threshold-based k-space division. Magn Reson Med. 2010; 63(5):1292–304. [PubMed: 20432300]

35. Salomir R, de Senneville BD, Moonen C. A fast calculation method for magnetic field inhomogeneity due to an arbitrary distribution of bulk susceptibility. Concepts in Magnetic Resonance Part B. 2003; 19:26–34.

36. Cheng Y, Neelavalli J, Haacke E. Limitations of calculating field distributions and magnetic susceptibilities in MRI using a fourier based method. Phys Med Biol. Mar; 2009 54(5):1169–89. [PubMed: 19182322]

37. de Rochefort L, Brown R, Prince MR, Wang Y. Quantitative MR susceptibility mapping using piece-wise constant regularized inversion of the magnetic field. Magn Reson Med. 2008; 60(4): 1003–9. [PubMed: 18816834]

38. Liu C, Li W, Johnson G, Wu B. High-field (9.4 T) MRI of brain dysmyelination by quantitative mapping of magnetic susceptibility. Neuroimage. Jun.2011 56(3):9308.

39. Shmueli K, de Zwart J, van Gelderen P, Li T, Dodd S, JH JD. Magnetic susceptibility mapping of brain tissue in-vivo using MRI phase data. Magn Reson Med. 2009; 62(6):1510–22. [PubMed: 19859937]

40. de Rochefort L, Liu T, Kressler B, Liu J, Spincemaille P, Lebon V, Wu J, Wang Y. Quantitative susceptibility map reconstruction from MR phase data using bayesian regularization: validation and application to brain imaging. MRM. Jan; 2010 63(1):194–206.

41. Schweser F, Deistung A, Lehr B, Reichenbach J. Differentiation between diamagnetic and paramagnetic cerebral lesions based on magnetic susceptibility mapping. Med Phys. 2010; 37(10)

42. Poynton, C.; Wells, W. A variational approach to susceptibility estimation that is insensitive to b0 inhomogeneity. Proceedings of the 19th Annual Meeting of ISMRM; Montreal, Canada. 2011;

43. Liu J, Liu T, de Rochefort L, Ledoux J, Khalidov I, Chen W, Tsiouris CWAJ, Spincemaille P, Prince M, Wang Y. Morphology enabled dipole inversion for quantitative susceptibility mapping using structural consistency between the magnitude image and the susceptibility map. Neuroimage. Feb; 2012 59(3):2560–8. [PubMed: 21925276]

44. Liu T, Wisnieff C, Lou M, Chen W, Spincemaille P, Wang Y. Nonlinear formulation of the magnetic field to source relationship for robust quantitative susceptibility mapping. Magn Reson Med. Apr.2012 in press.

45. Li J, Chang S, Liu T, Wang Q, Cui D, Chen X, Jin M, Wang B, Pei M, Wisnieff C, Spincemaille P, Zhang M, Wang Y. Reducing the object orientation dependence of susceptibility effects in gradient echo MRI through quantitative susceptibility mapping. Magn Reson Med. Nov; 2012 68(5):1563–9. [PubMed: 22851199]

46. Kressler B, de Rochefort L, Liu T, Spincemaille P, Jiang Q, Wang Y. Nonlinear regularization for per voxel estimation of magnetic susceptibility distributions from MRI field maps. IEEE Trans Med Imaging. Feb.2010 29(2):273–281. [PubMed: 19502123]

47. Bhagwandien R, Moerland M, Bakker C, Beersma R, Lagendijk J. Numerical analysis of the magnetic field for arbitrary magnetic susceptibility distributions in 2d. Magn Reson Imaging. 1992; 10(2):299–313. [PubMed: 1564997]

48. Bhagwandien R, Moerland M, Bakker C, Beersma R, Lagendijk J. Numerical analysis of the magnetic field for arbitrary magnetic susceptibility distributions in 3d. Magn Reson Imaging. 1994; 12(1):101–7. [PubMed: 8295497]

49. Collins C, Yang B, Yang Q, Smith M. Numerical calculations of the static magnetic field in three-dimensional multi-tissue models of the human head. Magn Reson Imaging. 2002; 20(5):413–24. [PubMed: 12206867]

50. Li S, Dardzinski B, Collins C, Yang Q, Smith M. Three-dimensional mapping of the static magnetic field inside the human head. Magn Reson Med. 1996; 36(5):705–14. [PubMed: 8916021]

51. Truong T, Clymer B, Chakeres D, Schmalbrock P. Three-dimensional numerical simulations of susceptibility-induced magnetic field inhomogeneities in the human head. Magn Reson Imaging. 2002; 20(10):759–70. [PubMed: 12591571]

52. Jenkinson M, Wilson J, Jezzard P. Perturbation method for magnetic field calculations of nonconductive objects. MRM. Sep; 2004 52(3):471–477.

53. Marques J, Bowtell R. Evaluation of a fourier-based method for calculating susceptibility induced magnetic field perturbations. Proc ISMRM. 2003; 11:1020.

54. Marques J, Bowtell R. Application of a fourier-based method for rapid calculation of field inhomogeneity due to spatial variation of magnetic susceptibility. Concepts in Magnetic Resonance Part B. 2005; 25(1):6578.

55. Poynton, C. Ph.D. dissertation. Massachusetts Institute of Technology; Feb.. 2012 Quantitative susceptibility mapping and susceptibility-based distortion correction of echo planar images.

56. Konzbul P, Sveda K. Shim coils for NMR and MRI solenoid magnets. Meas Sci Technol. 1995; 6:1116–1123.

57. Clare S, Evans J, Jezzard P. Requirements for room temperature shimming of the human brain. MRM. 2006; 55:210–214.

58. Li L, Leigh J. Quantifying arbitrary magnetic susceptibility distributions with MR. Magn Reson Med. May.2004 51(5):10771082.

59. Pohl K, Bouix S, Kikinis R, Grimson W. Anatomical guided segmentation with nonstationary tissue class distributions in an expectation-maximization framework. ISBI. 2004:81–84.

60. Zollei L, Shenton M, Wells W, Pohl K. The impact of atlas formation methods on atlas-guided brain segmentation. workshop at MICCAI. 2007

61. Poynton C, Jenkinson M, Wells W. Atlas-based improved prediction of magnetic field inhomogeneity for distortion correction of EPI data. LNCS, MICCAI. 2009; 12:951–9.

62. Fonov V, Evans AC, Botteron K, Almli CR, McKinstry RC, Collins DL. Unbiased average age-appropriate atlases for pediatric studies. NeuroImage. 2011; 54(1):313327.

63. Weisskoff R, Kiihne S. Quantitative susceptibility map reconstruction from MR phase data using bayesian regularization: validation and application to brain imaging. MRM. Apr; 1992 24(2):375–83.

64. Jenkinson M. Fast, automated, n-dimensional phase-unwrapping algorithm. MRM. 2003; 49(1):193–7.

65. Mattis, S. Psychological Assessment Resources. Odessa, FL: 1988. Dementia rating scale.

66. Smith S. Fast robust automated brain extraction. Human Brain Mapping. 2002; 17:143–155. [PubMed: 12391568]

67. Rohlfing T, Jr CM. Nonrigid image registration in shared-memory multiprocessor environments with application to brains, breasts, and bees. IEEE Trans. Inf. Technol. Biomed. 2003; 7:16–25. [PubMed: 12670015]

68. Rohlfing T, Zahr N, Sullivan E, Pfefferbaum A. The SRI24 multichannel atlas of normal adult human brain structure. Hum Brain Mapp. 2010; 31:798819.

69. Bartzokis G, Tishler T, Lu P, Villablanca P, Altshuler L, Carter M, Huang D, Edwards N, Mintz J. Brain ferritin iron may influence age- and gender-related risks of neurodegeneration. Neurobiology of Aging. 2007; 28(3):414–23. [PubMed: 16563566]

70. Ogg R, Langston J, Haacke E, Steen R, Taylor J. The correlation between phase shifts in gradient-echo MR images and regional brain iron concentration. Magn. Reson. Imaging. 1999; 17:11411148.

71. Lancaster J, Woldorff M, Parsons L, Liotti M, Freitas C, Rainey L, Kochunov P, Nickerson D, Mikiten S, Fox P. Automated talairach atlas labels for functional brain mapping. Human Brain Mapping. Jul.2000 10(3):120–131. [PubMed: 10912591]

72. Berg D, Roggendorf W, Schrder U, Klein R, Tatschner T, Benz P, Tucha O, Preier M, Lange K, Reiners K, Gerlach M, Becker G. Echogenicity of the substantia nigra: association with increased iron content and marker for susceptibility to nigrostriatal injury. Arch Neurol. Jun.2002 59(6):999–1005. [PubMed: 12056937]

73. Lotfipour A, Wharton S, Schwarz S, Gontu V, Schfer A, Peters A, Bowtell R, Auer D, Gowland P, Bajaj N. High resolution magnetic susceptibility mapping of the substantia nigra in parkinson's disease. J Magn Reson Imaging. 2012; 35(1):48–55. [PubMed: 21987471]

74. Wharton S, Bowtell R. Whole-brain susceptibility mapping at high field: a comparison of multiple- and single-orientation methods. Neuroimage. 2010; 53(2):515–25. [PubMed: 20615474]

75. Lee J, Shmueli K, Fukunaga M, van Gelderen P, Merkle H, Silva A, Duyn J. Sensitivity of MRI resonance frequency to the orientation of brain tissue microstructure. Proc Natl Acad Sci U S A. 2010; 107(11):5130–5. [PubMed: 20202922]

76. van der Knaap, M.; Valk, J. Myelin and White Matter, Magnetic resonance of myelination and myelin disorders. 2nd ed.. Springer; 2005.

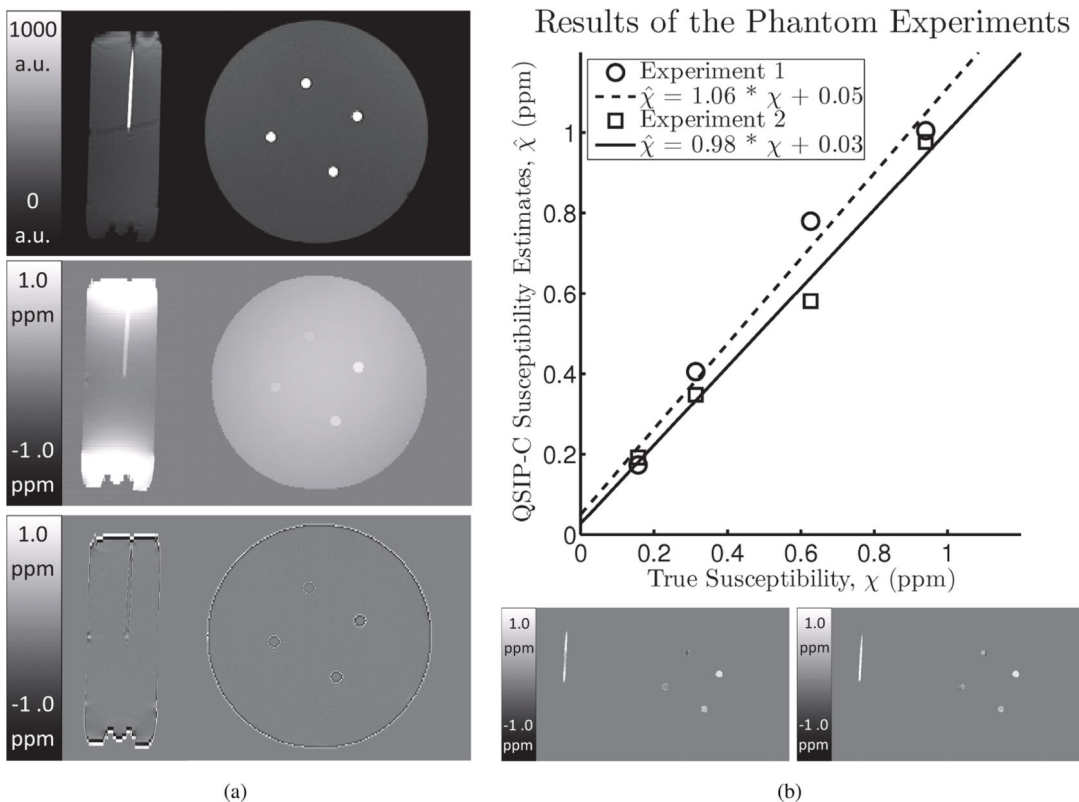77. Jackson, J. Classical Electrodynamics. 3rd ed.. Vol. 67. Wiley; 1999.

Fig. 1.
Results of the Phantom Experiments. Column (a) shows axial and sagittal cross-sections of the magnitude (row 1), fieldmap (row 2) and Laplacian of the fieldmap (row 3). Magnitude values appear homogeneous in the four tubes, while the fieldmap shows increasing contrast as a function of increasing gadolinium concentration. Applying the Laplacian to the fieldmap eliminates the substantial background field from external sources (i.e. air and shim). QSIP-C results show strong agreement with ground truth susceptibility values in column (b), with a slope of 1.06 and 0.98 for experiments 1 and 2, respectively. The axial cross-sections in column (b) also show increasing contrast with increasing gadolinium concentration in both experiment 1 (left) and 2 (right). The scale of the magnitude data is [0,1000] arbitrary units (a.u.) and all other images are shown on a scale of [-1,1] parts per million (ppm).
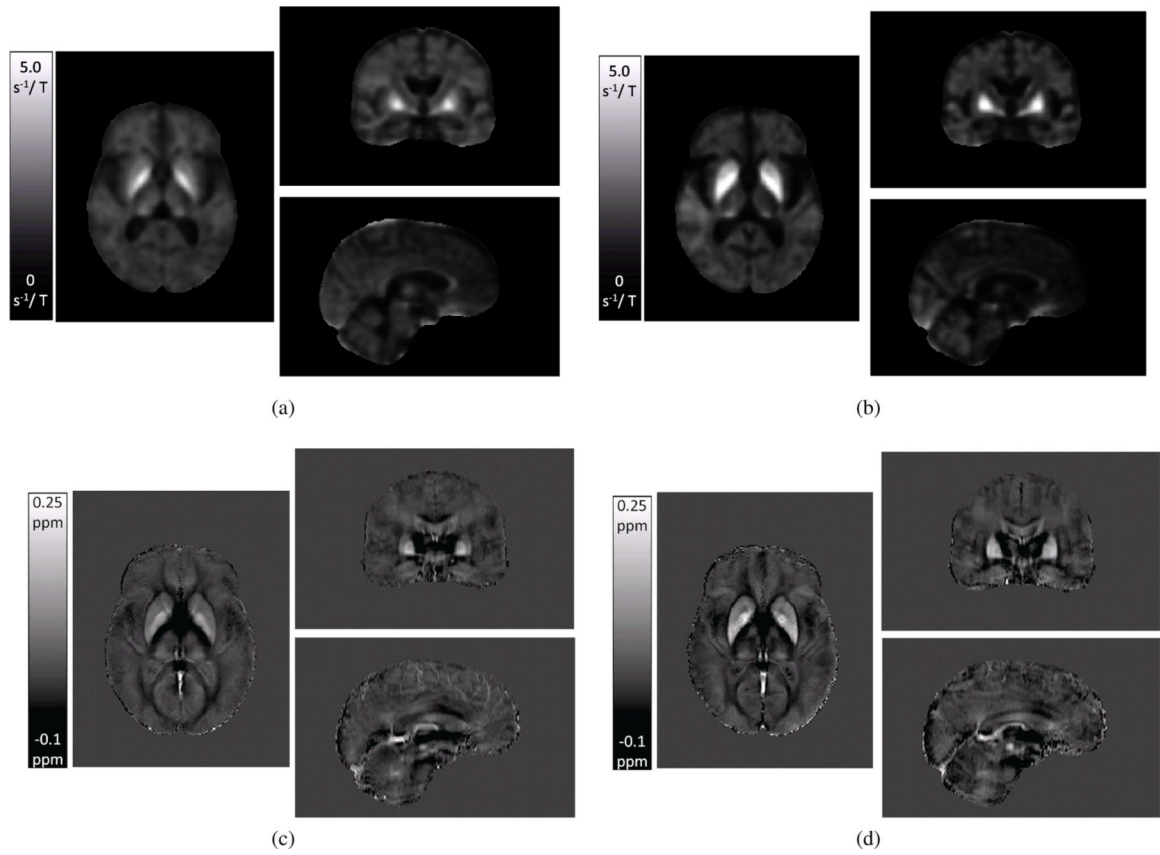
Fig. 2.
Young (a) and elderly (b) group averages of FDRI and young (c) and elderly (d) group averages of QSIP results. Greater iron concentration yields brighter FDRI and QSIP images.
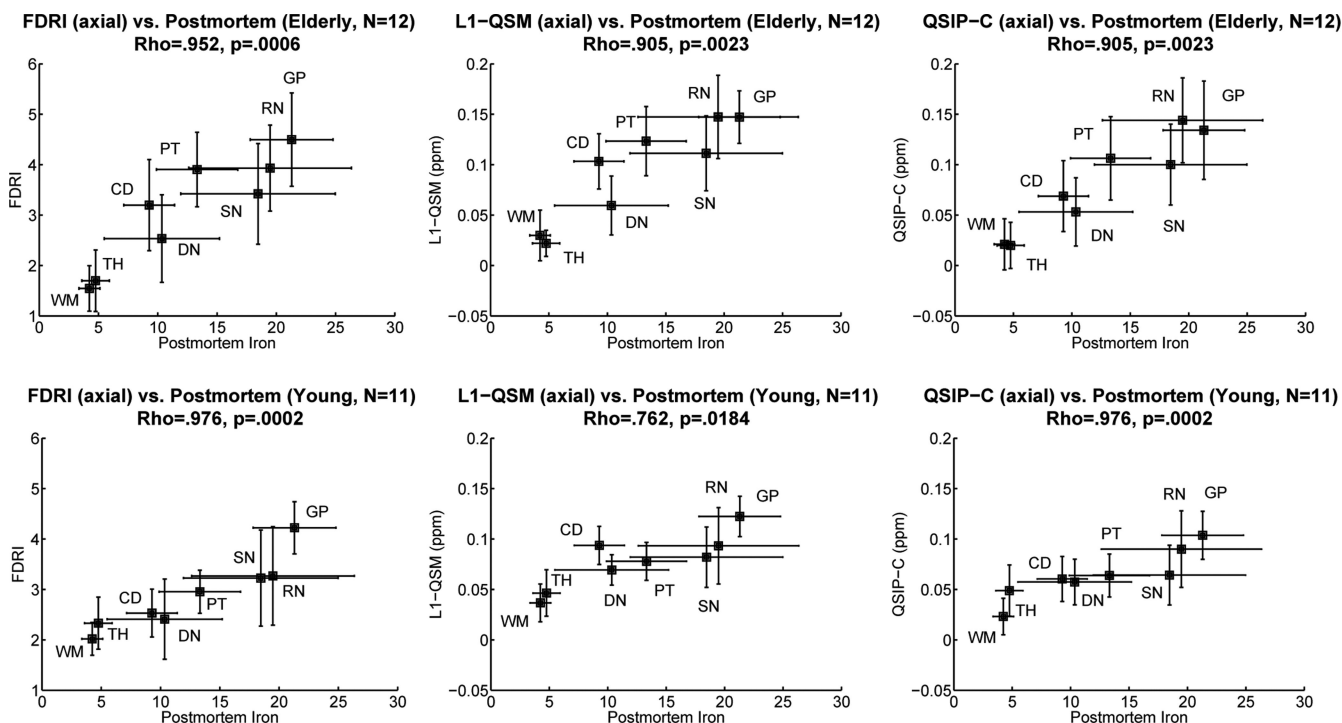
Fig. 3.

X-axis: Mean ± SD iron concentration (mg/100 g fresh weight) determined *postmortem* in each ROI [8]. *Y-axis*: Mean SD FDRI in s^{-1}/T (left), L1-QSM in ppm (middle) and QSIP-C in ppm (right) in phase-guided (axial) ROIs in 12 elderly (top) and 11 young (bottom) subjects. *ROIs:* frontal white matter (WM), thalamus (TH), dentate nucleus (DN), caudate (CD), putamen (PT), substantia nigra (SN), red nucleus (RN), and globus pallidus (GP).
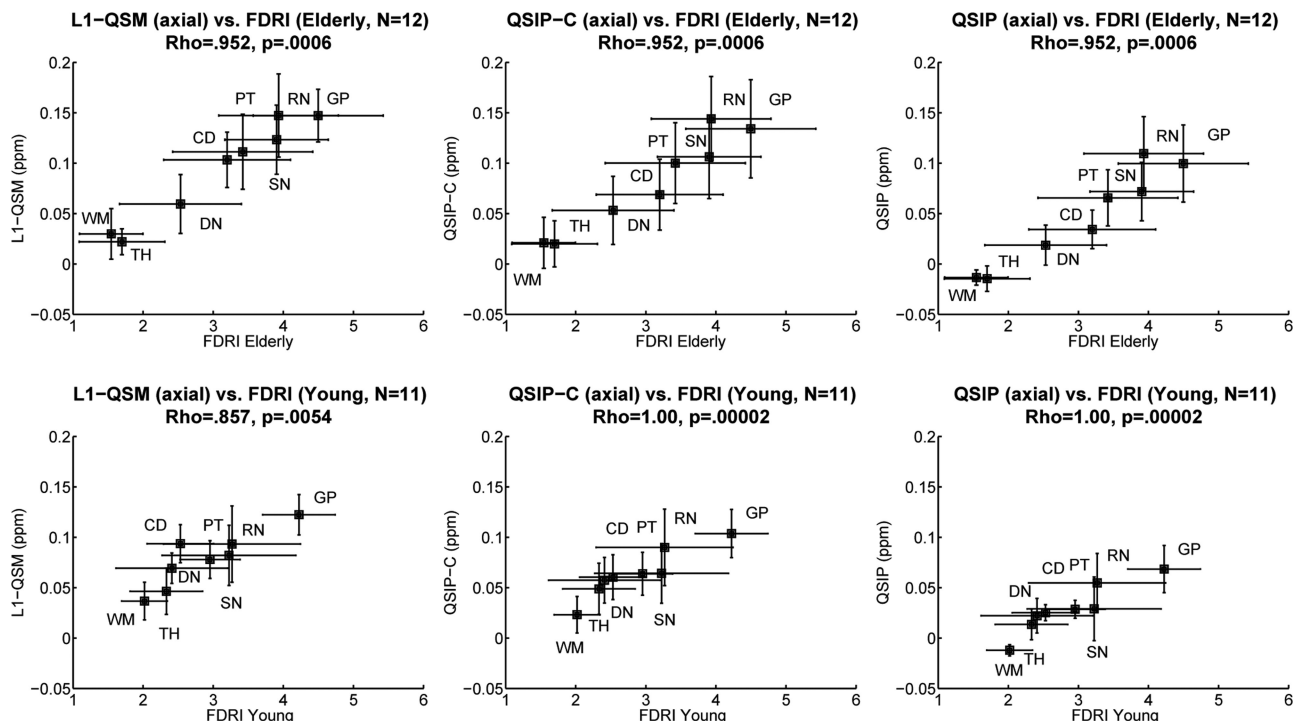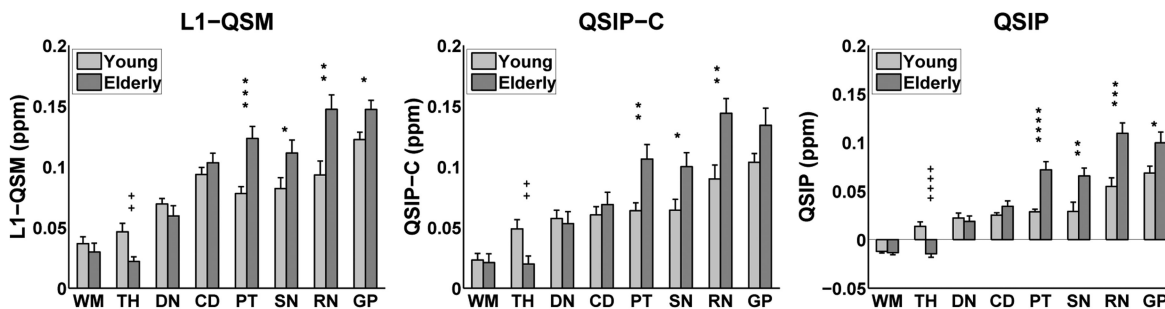
Fig. 4.
Correlations between Mean ± SD FDRI in s^{-1}/T and L1-QSM in ppm (left), QSIP-C in ppm (center), and QSIP in ppm (right) in 12 elderly (top) and 11 young (bottom) subjects using phase-guided (axial) ROIs. QSIP shows strong correlation with the FDRI, and QSIP results without baseline correction show smaller variance than L1-QSM in 7 of the 8 ROIs.

+ p<.05, ++ p<.01, +++ p<.001, ++++ p<.0001, Young > Elderly
∗ p<.05, ∗∗ p<.01, ∗∗∗ p<.001, ∗∗∗∗ p<.0001, Elderly > Young

Fig. 5.
Mean ± S.E.M. of mean relative susceptibility (ppm) in L1-QSM (left), QSIP-C (center) and QSIP (right) using phase-guided ROIs. Without baseline correction, QSIP measurements have lower absolute values, but also reduced variance, which increases the statistical significance of group differences. To assess group differences, p-values were calculated using a two-tailed t-test with $\alpha = 0.05$. Directional hypotheses regarding group differences were considered significant for p ≤ 0.0125, the corresponding one-tailed, family-wise Bonferroni-corrected p-value for 8 measures.
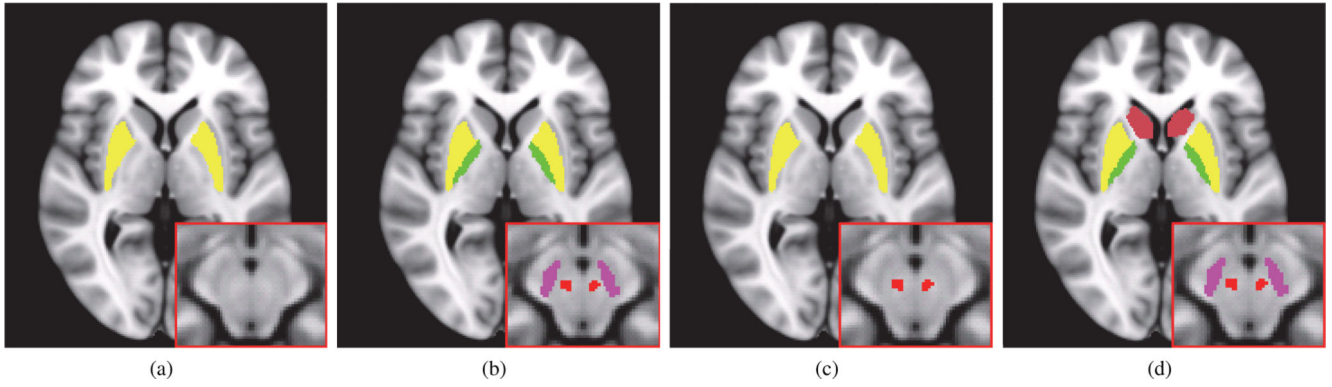
(a)   (b)   (c)   (d)

Fig. 6.
Summary of group differences. Statistically significant increases in ROI values in elderly relative to young subjects across all phase-guided and FDRI-guided ROIs is shown above in axial views of the cerebrum and brainstem (red box). ROIs obtained from a standard Talairach atlas [71] are overlaid on the MNI152T1 atlas [62] for visualization purposes only. Numerical results of all t-tests (requiring p 0.0125 for significance under one-tailed, Bonferroni-correction for 8 comparisons) are provided in tables 1-4 of the supplemental material. QSIP (d) showed statistically significant increases in QSM values in all five striatal and brain stem nuclei: putamen (yellow), caudate (maroon), globus pallidus (green), red nucleus (red), and substantia nigra (purple), consistent with hypothesized age-dependent iron deposition in these regions. Results for FDRI (a), L1-QSM (b), and QSIP-C (c) show group differences in fewer regions, which may be due to greater variabiliy in ROI estimates obtained with these methods.